

# Dynamical Properties of Molecular Cloud Complexes in a Redshift 6 Prototypical Galaxy at the Epoch of Reionization

T. K. Daisy Leung<sup>1, 2</sup>, Andrea Pallottini<sup>3, 4</sup>, Andrea Ferrara<sup>4, 5</sup>, and Mordecai-Mark Mac Low<sup>2, 6, 7</sup>

<sup>1</sup> Department of Astronomy, Space Sciences Building, Cornell University, Ithaca, NY 14853, USA; tleung@astro.cornell.edu

<sup>2</sup> Center for Computational Astrophysics, Flatiron Institute, 162 Fifth Avenue, New York, NY 10010, USA

<sup>3</sup> Centro Fermi, Museo Storico della Fisica e Centro Studi e Ricerche “Enrico Fermi”, Piazza del Viminale 1, Roma, 00184, Italy

<sup>4</sup> Scuola Normale Superiore, Piazza dei Cavalieri 7, I-56126 Pisa, Italy

<sup>5</sup> Kavli Institute for the Physics and Mathematics of the Universe (IPMU), The University of Tokyo, 5-1-5 Kashiwanoha, Kashiwa 277-8583, Japan

<sup>6</sup> Institut für Theoretische Astrophysik, Zentrum für Astronomie der Universität Heidelberg, 69120 Heidelberg, Germany

<sup>7</sup> American Museum of Natural History, 79th St. at Central Park West, New York, NY 10024, USA

*Paper draft for the project developed at the Kavli Summer Program in Astrophysics 2018. To be Submitted.*

## Abstract

We study the dynamical properties of molecular clouds complexes (MC) and their temporal evolution in Althæa, a prototypical galaxy at the Epoch of Reionization (EoR) using cosmological zoom-in simulation. We use a clump-finding algorithm and a set of H<sub>2</sub> volumetric densities ( $n_{\text{cut}}$ ) to identify MCs and their sub-structures. We extract properties such as mass, size, velocity dispersion, gas surface density, and virial parameter ( $\alpha_{\text{vir}}$ ) for each MC and compare them with those observed in the Milky Way disk, the Galactic center, and gas-rich starburst galaxies in the local Universe and at the peak epoch of cosmic star formation. The high velocity dispersions found in the MCs of Althæa ( $\sigma \approx 200 \text{ km s}^{-1}$ ) are comparable to those observed in starburst galaxies. The mass scale of the MCs is on the order of  $10^{6.5-9} M_{\odot}$ . The  $\sim 200 \text{ pc}$ -scale MCs found with a low density threshold correspond to the spiral arms of Althæa which break down into smaller  $\lesssim 100 \text{ pc}$ -scale MCs at higher density thresholds. The more massive and bigger MCs in Althæa compared to the Milky Way likely result from the higher gas mass fraction, surface density, and velocity dispersion, which set the scale for fragmentation. The MCs of Althæa are found to have higher  $\sigma$  and  $\Sigma$  systematically regardless of the  $n_{\text{cut}}$  adopted, with  $\sigma \gtrsim 100 \text{ km s}^{-1}$  even when we increase the  $n_{\text{cut}}$  and even for the molecular substructures. The high velocity dispersions likely result from the strong supernova and stellar feedback Althæa experienced over the multiple episodes of bursty star formation. Virial analysis indicates that the MCs found in the main disk of Althæa are unbound, but its substructures have lower virial parameters. This is consistent with the notion that collapsing structures result from gravitational instability within globally stable structures, which are supported by turbulence and rotation on large scale. We find  $\alpha_{\text{vir}} \approx 2$  for the MCs in the satellite galaxies, which we interpret as result of the weaker stellar feedback due to the less frequency star formation compared to Althæa (also supported by the lower stellar-to-gas mass ratio of the former). MCs in the satellites are therefore likely collapsing structures. This paints a picture, in which at the EoR, star formation continues as gas is being accreted from the intergalactic medium. We find no temporal variations in the MC dynamics over the course of 700 Myr traced in our simulation, at least in terms of the scaling relations examined. Our results are insensitive to the choice of  $n_{\text{cut}}$ , except for the slope of the cumulative mass distribution, which steepens with  $n_{\text{cut}}$ . High resolution imaging of the first galaxies with the Atacama Large (sub-)Millimeter Array (ALMA) and the Next Generation Very Large Array (ngVLA) will provide useful observational data to test our findings and the validity of our simulation to shed light on star formation since the cosmic dark ages.

**Keywords:** methods: data analysis – galaxies: high-redshift – galaxies: ISM – galaxies: evolution – galaxies: formation – galaxies: starburst – stars: formation

## 1. Introduction

The growth of galaxies and their subsequent evolution are governed by the baryon cycle — galaxies accrete gas from the intergalactic medium (IGM) to fuel star formation (and feed their supermassive blackholes) and subsequent feedback replenishes and enriches the circumgalactic medium with part of this material. The general consensus is that the growth of high- $z$  galaxies are triggered and supported by massive gas inflows from mergers and/or the cosmic web at early cosmic time, when the IGM and galaxies themselves are more

gas-rich in their star-forming molecular gas contents compared to present-day galaxies. These massive gas inflows in turn trigger gravitational instability and lead to the formation of gas structures that are typically more massive and denser than those observed in nearby galaxies, with masses of  $M_{\text{cl}} = 10^9 M_{\odot}$  and sizes on sub-kpc scales (e.g., Gabor & Bournaud 2013; Hopkins et al. 2014; Inoue et al. 2016). Some theoretical works argue that the migration of such giant massive clumps are responsible for contributing to the buildup of the bulges of massive galaxies at  $z \sim 0$  (e.g., Ceverino et al. 2010).

Given that high- $z$  galaxies are the early stages of evolution of present-day galaxies, studying their ISM properties is essential for understanding how star formation proceed under these relatively more extreme conditions, thereby driving the evolution and assembly of galaxies since the cosmic dark ages. Current consensus is that at higher redshifts, galaxies have higher star formation rates (SFR; Behroozi et al. 2013; Sparre et al. 2015; Maiolino et al. 2015; Dunlop et al. 2017) and smaller sizes (e.g., Bouwens et al. 2011; Ono et al. 2013) compared to those found in the local Universe. The former are thus expected to have more H II regions, ionized gas, and more intense radiation stellar feedbacks. Since their metallicity and dust content are also expected to be lower as they are assembling, this affects the shielding of UV photons, heating and cooling mechanisms in these early systems. Such differences in turn affect the regulation of thermal and chemical structures of their ISM. Their multi-phase ISM and the dynamics of the star-forming molecular cloud complexes (MC) are therefore expected to differ from nearby galaxies. Even in the local Universe, where the most detailed observations can be attained, variations in cloud properties have been observed between different galaxy populations (see e.g., Hughes et al. 2010, 2013). It is thus intuitive and reasonable to pose the question: what are the dynamical states of the MCs of the first galaxies and how do they differ from the local Universe, and are they analogous to any seen in the local galaxy populations?

The FIR fine-structure lines (e.g., [CII], [NII], and [OIII]), and CO/[CI] lines are the key diagnostics for constraining the ISM conditions of galaxies and provide highly complementary information tracing the different phases of the ISM (ionized, atomic, molecular; e.g., Scoville & Solomon 1974; Rubin 1985; Malhotra et al. 2001). Global measurements of these diagnostics in high- $z$  galaxies have informed us on their galaxy-wide properties (e.g., gas masses, gas temperature, and radiation field intensity). However, spatially resolving their ISM is necessary to understand their roles in galaxy evolution and the physics behind their intense star formation ( $\text{SFR} \sim 100 - 3000 M_{\odot} \text{ yr}^{-1}$ ). To date, spatially resolved ISM properties of high- $z$  galaxies have only been examined observationally in a handful of (strongly-lensed) galaxies, using tracers such as dust continuum, CO, and [CII] lines (e.g., Swinbank et al. 2011; Hodge et al. 2015; Ferkinhoff et al. 2015; Hodge et al. 2016, Leung et al. 2018, submitted). These studies find that galaxies at  $z \sim 2$  galaxies, close to the peak of cosmic star formation, are more molecular gas-rich, turbulent, and clumpy than nearby galaxies. That said, it remains unclear how star formation proceed in the (sub-) $L^*$  galaxy population at  $z \gtrsim 6$  — the epoch of reionization — which is responsible for producing the ionizing photons that reionized the Universe.

While ALMA has enabled the detections of ISM diagnostic lines e.g., the [CII] 158  $\mu\text{m}$  and CO line emission in normal ( $\text{SFR} < 100 M_{\odot} \text{ yr}^{-1}$ ) galaxies at  $z > 6$  over the past few years

(e.g., D’Odorico et al. 2018; Carniani et al. 2018), we are still far from mapping their molecular ISM due to the cosmological dimming. As such, we have undertaken a study, exploiting state-of-the-art cosmological zoom-in hydrodynamic simulation SERRA (Greenhouse in Italian; Pallottini et al. 2017b,a), to examine the dynamical properties of the molecular cloud complexes in a  $z \sim 6$  prototypical (i.e.,  $L^*$ ) galaxy.

This paper is structured as follows. In §2, we describe the setup of our simulation and properties of our main galaxy (Althaea), and describe the method used to identify its molecular gas complexes. In §3, we present scaling relations based on the MC identified and compare them with observations of molecular clouds and structures seen in nearby and  $z > 0$  galaxies. We discuss the results and implications of our findings in §4, and present our conclusions in §5. Throughout this paper, we adopt a concordance cosmology, with total matter, vacuum and baryonic densities in units of the critical density  $\Omega_{\Lambda} = 0.692$ ,  $\Omega_m = 0.308$ ,  $\Omega_b = 0.0481$ , Hubble constant  $H_0 = 100 h \text{ km s}^{-1} \text{ Mpc}^{-1}$  with  $h = 0.678$ , spectral index  $n = 0.967$  and  $\sigma_8 = 0.826$  (Planck Collaboration et al. 2014).

## 2. Method: Simulation and “Clump”-finding

### 2.1. SERRA Simulation<sup>7</sup>

The simulation used in this work is described by Pallottini et al. 2017b,a and is briefly summarized here.

SERRA is a cosmological zoom-in simulation performed using Eulerian hydrodynamics and adaptive mesh refinement (AMR) technique to achieve high spatial resolution in the region of interest (i.e., regions of high density). In particular, it uses a modified version of RAMSES (Teyssier 2002) as the AMR backend. Our simulation covers a co-moving box of  $20 \text{ Mpc } h^{-1}$  in size, resolving down to a physical scale of  $l \approx 30 \text{ pc}$  (at  $z \sim 6$ ) and a (baryonic) mass resolution of  $m_b \simeq 10^4 M_{\odot}$  at the finest level. Such a physical scale is close to the size scale of molecular cloud complexes and giant molecular clouds (GMCs) seen in nearby galaxies (e.g., Sanders et al. 1985; Federrath & Klessen 2013; Goodman et al. 2014). We include chemical network in the simulation to trace H,  $\text{H}^+$ ,  $\text{H}^-$ , He,  $\text{He}^+$ ,  $\text{He}^{++}$ ,  $\text{H}_2$ ,  $\text{H}_2^+$  (Grassi et al. 2014; Bovino et al. 2016). Of particular importance to our study here is that our simulation includes non-equilibrium formation of molecular hydrogen (done on-the-fly) to determine the  $\text{H}_2$  abundance (see Pallottini et al. 2017a for effects of chemistry affected by non-equilibrium versus equilibrium  $\text{H}_2$  formation).

Star formation is modeled using a  $\text{H}_2$ -based prescription of the Schmidt-Kennicutt relation (Krumholz et al. 2009). We adopt stellar tracks from STARBURST99 and include stellar feedback from supernovae and OB/AGB stars to account for energy dissipations. To couple the feedback to the gas, we employ sub-grid modeling for blastwaves, e.g., to account for

<sup>7</sup> Serra means greenhouse in Italian which is motivated by the fact that our simulation includes a chemical network to calculate the abundance of  $\text{H}_2$ , which in turn dictates the formation of CO.

the potential lost of energy inside the cell during a supernova explosion. The energy dissipated is then injected into the ISM in the form of kinetic and thermal energies. Radiation pressure on the dust and gas is also included (see Pallottini et al. 2017b for details).

Details on the properties of Althæa — the main galaxy in our simulation — are discussed in Pallottini et al. (2017a). Briefly, by  $z \sim 6$ , Althæa is a Lyman-break galaxy (LBG), hosted in a dark matter halo of mass  $M_{\text{DM}} \simeq 10^{10} M_{\odot}$  at the center of a cosmic web knot, and accretes mass from the IGM mainly via three filaments of length  $\simeq 100$  kpc. At  $z \sim 6$ , Althæa has a stellar mass of  $M_* \simeq 3 \times 10^{10} M_{\odot}$ , a metallicity of  $Z \simeq 0.5 Z_{\odot}$ , a molecular gas mass of  $M_{\text{H}_2} \simeq 5 \times 10^7 M_{\odot}$ , and a globally-integrated SFR of  $\simeq 100 M_{\odot} \text{ yr}^{-1}$ . It is therefore a prototypical galaxy at  $z \sim 6$ .

The simulation data contain information such as the density ( $\rho$ ) and velocity ( $v_x$ ,  $v_y$ , and  $v_z$ ) fields, from which we calculate the physical properties of each MC, such as mass and velocity dispersion. Due to the nature of our AMR simulation, we regrid the simulation data into uniform grids for the analysis presented in this paper. The grid size is defined based on the highest resolution of the simulation data (i.e., the less refined regions are supersampled in the resulting uniform grids).

## 2.2. Star Formation History

One of the main advantages for studying the dynamical properties of molecular structures at  $z \sim 6$  in simulation is the fact that we can examine how their properties evolve as a function of time. This is advantageous especially at early cosmic epochs, when the densest structures are beginning to form; gas is constantly being accreted onto the central galaxy from the cosmic web and satellite galaxies, thereby leading to bursts of star formation. Meanwhile, tidal forces resulting from interactions with these surrounding galaxies can disrupt the main disk and arms, likely leading to different dynamical states for the molecular structures compared to more evolved galaxies found at a later cosmic time (e.g., some molecular structures may disperse while others may agglomerate into more massive ones).

We show the star formation history of Althæa in Figure 1, where the SFR of Althæa varies between  $\sim 30 - 80 M_{\odot} \text{ yr}^{-1}$ <sup>8</sup> as it evolves from an actively accreting phase to a starburst phase after a major merger, and then back to a relatively quiescent phase over the few hundred Myr simulated in our simulation. The SFR of Althæa is calculated based on existing young stellar population, which is defined to have an age of  $t_{\text{age}} < 10$  Myr.

Given the stochasticity in the star formation history of Althæa, we show the scaling relations found for two particular snapshots/evolutionary stages of Althæa as examples in

<sup>8</sup> The SFR plotted in Figure 2 of Pallottini et al. (2017a) is a factor of two higher than shown here since they also include contributions from massive satellite galaxies within the surrounding  $\approx 50$  kpc, which are accreted onto Althæa at  $z \lesssim 2$ .

§3.2.1 to illustrate the salient points of the discussion presented in this paper, since they represent the extreme evolutionary stages of Althæa (and thus, likely bracket the most extreme variations in the cloud dynamics) — one of which Althæa is actively accreting materials from its surrounding and another of which Althæa is undergoing a starburst phase after a major merger (see Figure 1).

## 2.3. Structure identification

To identify the molecular complexes, we use a customized version of the clump-finding algorithm available in the PYTHON package YT (Turk et al. 2011), which was initially described in Smith et al. (2009), but this function has been modified since then. The latest version of the default YT clump finder decomposes the zones in the simulation into non-overlapping tiles, which are stored in a k-dimensional tree (k-d tree). It then identifies the contours of a variable field (here, the density field) within a tile and connects them across the tiles. In the customized version used for this study, we modify the function to enhance the stability of the code.

In the “clump-finding” process, we employ a set of different density thresholds defined based on the molecular hydrogen density of Althæa taken at different cosmic times (between  $z = 6.0 - 7.2$ ). We note that this process is in essence similar to identifying molecular structures based on the noise levels of surface density maps observers obtain with telescopes, using molecular line tracers such as CO, CS, and HCN, as commonly adopted in observational studies (e.g., identifying “clumps” based on/after applying  $\sigma$ -clipping, using tools such as AIPS’s task SERCH, CLUMPFIND, and CPROPS; Williams et al. 1994; Oka et al. 2001; Rosolowsky & Leroy 2006; Rosolowsky et al. 2008). We note that, owing to the nature of observations, such structures are identified in position-position-velocity (PPV) space, whereas in simulations, one has the full 6D spatial-kinematic information, and can therefore cleanly identify structures directly using the density field in position-position-position (PPP) space. Existing studies find a good correspondence in the dynamical properties extracted in PPV- versus PPP-space (Ballesteros-Paredes & Mac Low 2002; Heitsch et al. 2009; Shetty et al. 2010; Beaumont et al. 2013; Pan et al. 2015, but see also Shetty et al. 2010 for a discussion on caveats and limitations).

In Figure 2, we show an example of the volumetric  $\text{H}_2$  density ( $n_{\text{H}_2}$ ) distribution of Althæa for a given snapshot which includes contributions within  $R \sim 3.5$  kpc from the galaxy center<sup>9</sup>. We note that the distribution is almost flat for  $n_{\text{H}_2} \gtrsim 1 \text{ cm}^{-3}$  and it samples the range of density where “clumps/structures” are found based on the Euler characteristic, i.e., the fourth Minkowsky functional (see Pallottini et al. 2017a). We identify MCs by applying 10 equally-spaced volumetric  $\text{H}_2$  density cuts of  $\log(n_{\text{cut}}/\text{cm}^{-3}) \in$

<sup>9</sup> For reference, the half mass radius of Althæa is  $\sim 0.5$  kpc and the dark matter virial radius at which the mean enclosed density is 200 times the critical density of the Universe is  $r_{200} \sim 15$  kpc.

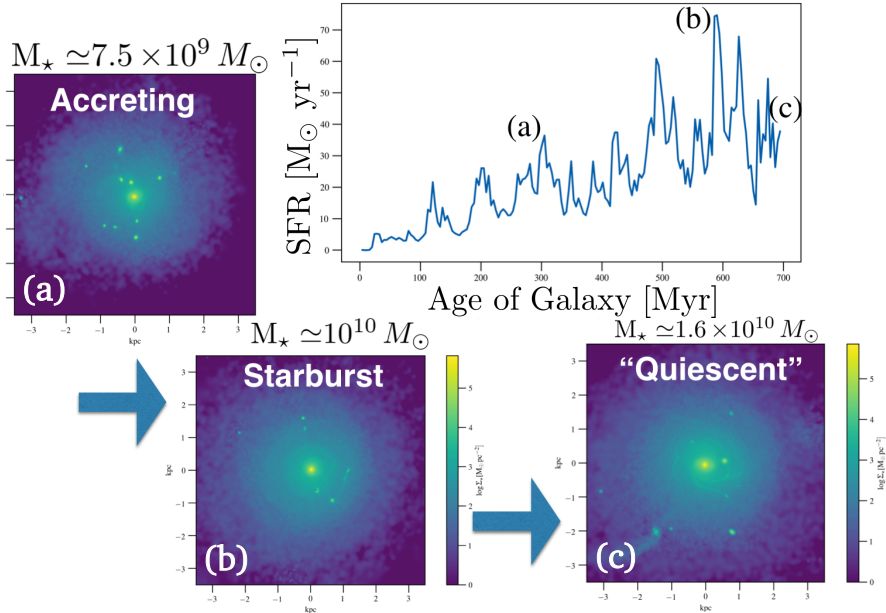


**Figure 1.** Star formation history of Althaea (top right) and projected stellar mass distribution of Althaea during one of its accretion phases at its early stage of evolution (a); during one of its major starburst phases after a major merger (b); and in a relatively quiescent phase post-starburst (c).

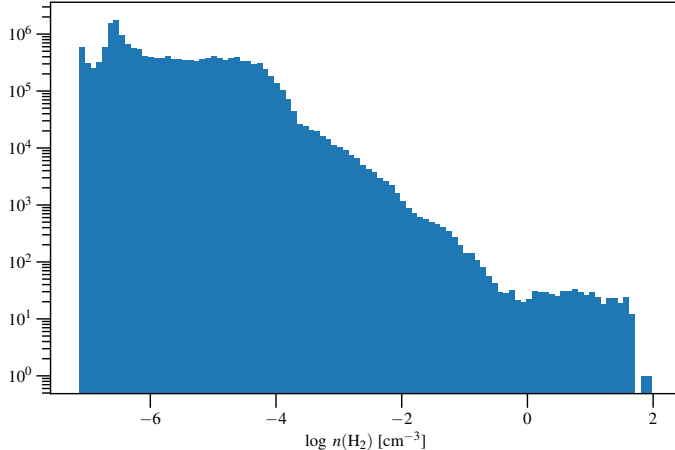


**Figure 2.** Volumetric H<sub>2</sub> density distribution of Althaea taken from a single snapshot, corresponding to the accretion phase shown in Figure 1.

$[-0.5, 1.5] = [0.32, 0.53, 0.88, 1.45, 2.45, 4.08, 6.81, 11.36, 19.00, 31.62]$ <sup>10</sup> to the same snapshot used to plot Figure 2.

For visualization, we overplot the molecular structures identified using a subset of the  $n_{\text{cut}}$  (0.53, 6.81, and 19.00 cm<sup>-3</sup>) on the H<sub>2</sub> density maps in Figure 3 as an example. The plots shown in Figure 3 are weighted by the column density of the total gas content.

Since the molecular structures identified could easily appear as overlapping structures depending on the viewing angle, we also plot them in different three-dimensional projections (right panels of Figure 3) — so that one can more easily see that they are collections of disjoint structures. We repeat this identification process for 14 snapshots between redshift  $z$

$\in [6.0, 7.2]$ , spaced by  $\Delta t = 50$  Myr.

Limited by the spatial resolution of our simulation ( $l_{\text{cell}} \simeq 30$  pc), we impose an addition constraint such that an identified structure only survives if it spans at least 10 cells in PPP space. We caution that one caveats of such constraint is that we can only examine the parameter space of “cloud” scaling relations at “cloud” size  $R \gtrsim 100$  pc.

### 3. Results: Cloud Scaling Relations

Molecular clouds are the natal place for star formation, and thus, their structure and dynamics hold important clues to understanding the mechanisms and physics of formation and evolution of molecular structures and star formation. Upon identifying the molecular structures, we extract properties such as mass ( $M_{\text{cl}}$ ), size ( $R$ ), Mach number ( $\mathcal{M}$ ), velocity dispersion ( $\sigma$ ), and gas surface density ( $\Sigma_{\text{gas}}$ ) to examine their dynamics.

The mass of an MC is calculated from the uniformly-gridded 3D density field, integrating over all zones of the MC, multiplied by its volume. The size of an MC ( $R$ ) is defined assuming spherical geometry (i.e., the size is parameterized via the radius of a sphere, which has a volume corresponding to that of the identified MC). Since in observations, dense gas contributes more to the observed linewidths than the more diffuse gas. We therefore calculate the non-thermal component of the velocity dispersion ( $\sigma_{\text{NT}}$ ) of each MC as a density-weighted quantity:

$$\sigma_{\text{NT}}^2 = \frac{1}{3} \frac{\sum_i \rho_i |\mathbf{v}_i - \bar{\mathbf{v}}|^2}{\sum_i \rho_i}, \quad (1)$$

which is summed over the cells composing each MC. The total velocity dispersion includes contributions from the thermal

<sup>10</sup> We also vary the range of  $n_{\text{cut}}$  adopted and find no qualitative differences affecting the results and conclusions of this work except in the slope of the CMF (see §4.1 and §3.2.2).

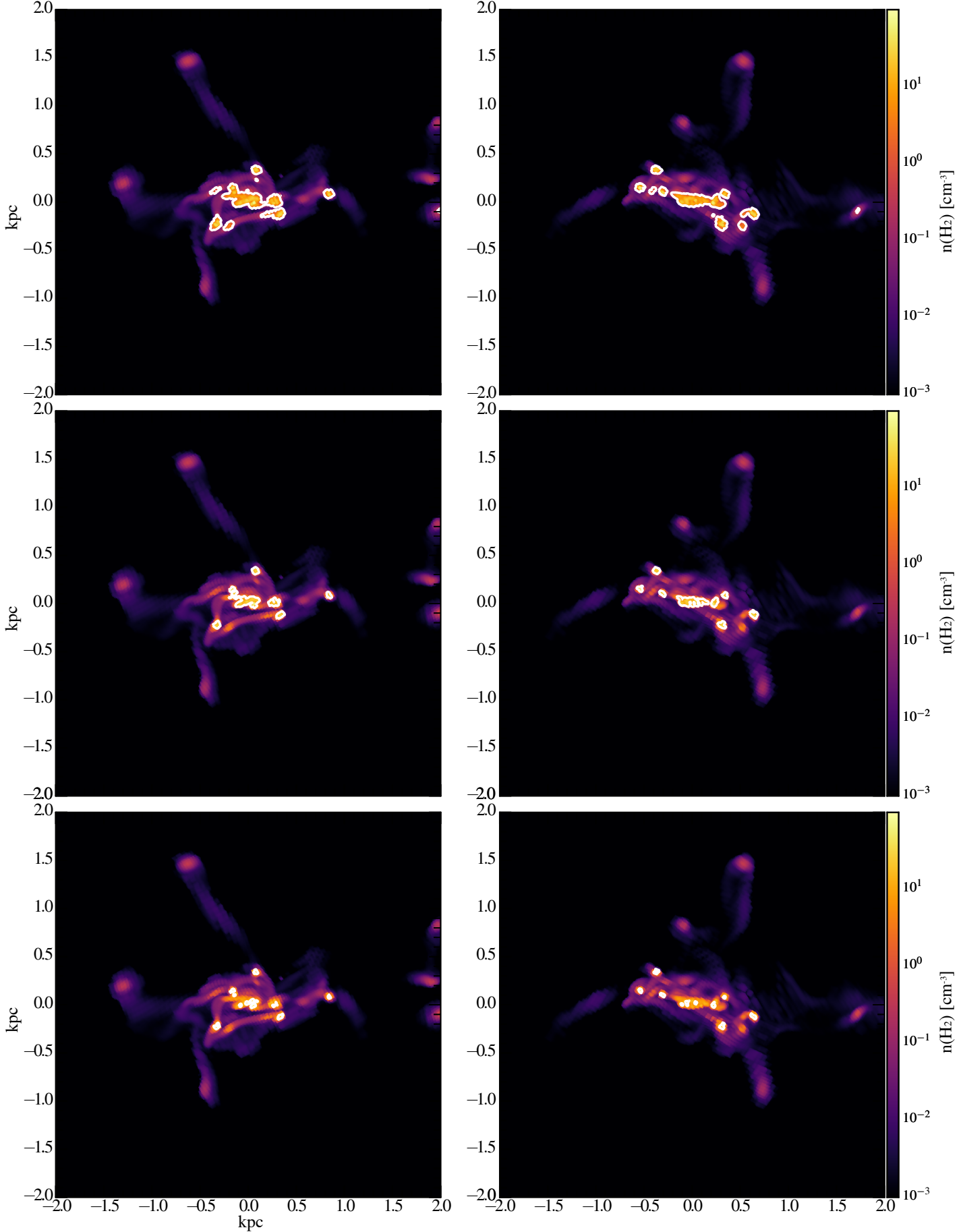


**Figure 3.** Examples showing the MCs identified in our simulation by applying volumetric  $\text{H}_2$  density cuts of  $n_{\text{cut}} = [0.53, 6.81, 19.00] \text{ cm}^{-3}$ , which is only a subset of all the  $n_{\text{cut}}$  adopted (see text). Color shows the  $\text{H}_2$  surface density, weighted by the column density.

sound speed ( $c_s$ ):

$$\sigma^2 = \sigma_{\text{NT}}^2 + c_s^2. \quad (2)$$

The local sound speed ( $c_s$ ) of all identified molecular complexes are generally much smaller compared to their turbulent velocities<sup>11</sup>. On average, the Mach number of the MCs corresponds to about  $\mathcal{M} \approx 50$ . This is consistent with the global analysis done on Althaea by Vallini et al. (2018).

We show in Figure 4 the MC distributions in terms of their molecular gas masses, radii, and gas mass fractions, which we define as

$$f_{\text{gas}} = \frac{M_{\text{H}_2}}{(M_{\text{H}_2} + M_*)}, \quad (3)$$

where  $M_*$  is the stellar mass. We note that the distributions vary for different snapshots, depending on the evolutionary stage of Althaea. The highest density threshold of  $n_{\text{cut}} = 31.62 \text{ cm}^{-3}$  yields a “minimum” MC mass of the order of  $10^{6.5} M_\odot$  for the densest MC. We find  $\sim 10 - 13$  MCs with masses exceeding  $10^8 M_\odot$  across all the snapshots for each of the given  $n_{\text{cut}}$  (see §2.3).

In the following subsections, we examine the MC properties in the context of the Larson’s relations (Larson 1981), which describe interactions between gravity and turbulence and is the first set of relations used for studying star-forming molecular structure formation based on observables (linewidth-size, density-size, and mass-size relations) and for comparing properties of molecular structures in different galactic environments. Observations of nearby gas-rich galaxies such as M64 and NGC 253 show higher velocity dispersions compared to the disk/mid-plane of the Milky Way which are, on the other hand, more consistent with those observed in the inner regions of Milky Way and M51 (Oka et al. 2001; Rosolowsky & Blitz 2005; Heyer et al. 2009; Hughes et al. 2013; Leroy et al. 2015; Rice et al. 2016). While the velocity dispersions of the clouds in these nearby gas-rich galaxies are comparable to the inner regions of Milky Way, they are found to be bigger in size (approximately an order of magnitude) and mass (approximately two orders of magnitude). These bigger clouds have been interpreted as a results of their higher gas mass fractions and surface densities and velocity dispersions, since fragmentation occurs near the Jeans length  $L_J \propto \sigma^2/\Sigma$  and Jeans mass  $M_J \propto \sigma^4/\Sigma$  for dispersion-supported structures.

### 3.1. Formalism: Virial Equilibrium and Larson’s Relations

A spherically symmetric cloud of mass  $M$  and radius  $R$  embedded within a medium of pressure  $P$  is described using the virial theorem:

$$\frac{1}{2}\ddot{I} = 2(T - T_s) + W + B, \quad (4)$$

<sup>11</sup> We find comparable velocity dispersion between that derived from taking the root mean square versus that derived from thermal and non-thermal pressure terms, indicating that rotation velocity is unlikely to be the dominant source of velocity dispersion reported here. In the subsequent sections, we adopt the root mean square of the velocity field as the velocity dispersion ( $\sigma$ ).

where  $\ddot{I}$  is the second time derivative of the Lagrangian moment of inertia,  $T$  is the volume term of the total kinetic energy (including thermal and bulk motions),  $T_s$  is the surface term due to external pressure,  $W$  is the gravity term, and  $B$  is the magnetic term. In the case where magnetic field is excluded (i.e.,  $B = 0$ ), we can express this in terms of:

$$\frac{1}{2}\ddot{I} = 3M\sigma^2 - \frac{\Gamma GM^2}{R} - 4\pi P_{\text{ext}}R, \quad (5)$$

where the first term on the right hand side (RHS) is the pressure term from velocity dispersion, the second term is the gravity term, and the third term is the external pressure term. For the case of simple virial equilibrium (SVE; i.e., equilibrium state without external pressure), the LHS and the last term on the RHS vanish. The equation becomes:

$$\alpha_{\text{vir}} = \frac{3\sigma^2}{\Gamma GM/R} = \frac{5\sigma^2 R}{GM}, \quad (6)$$

where  $\Gamma$  is set to 3/5 for a uniform sphere. We can define

$$V_0^2 \equiv \frac{\sigma^2}{R}, \quad (7)$$

which is related to one of the Larson’s relations (linewidth-size relation), which can be recast into the form of:

$$\sigma^2/R = \pi G \Sigma / 5. \quad (8)$$

For pressure-bounded virial equilibrium (PVE; i.e. equilibrium state with pressure), Equation 5 becomes

$$P_{\text{ext}} = \frac{3\sigma^2 M}{4\pi R^3} - \frac{\Gamma GM^2}{4\pi R^4}, \quad (9)$$

which describes the external pressure needed to confine the gas inside a volume  $V$ . Rearranging the equation and substituting  $\Sigma = M/\pi R^2$ , we can express this equation using the following:

$$\frac{\sigma^2}{R} = \frac{1}{3} \left( \frac{4P_{\text{ext}}}{\Sigma} + \Gamma G \Sigma \pi \right). \quad (10)$$

Therefore, for a virialized cloud, one expects a one-to-one mapping between  $V_0^2$  and  $\Sigma$  since  $\sigma^2/R \propto \Sigma$ , whereas Equation 10 represents the loci along which external pressures  $P_{\text{ext}}$  are needed in order for MCs to have linewidths  $\sigma$  for a given set of surface densities (see bottom panels of Figure 6 and Figure 7). In other words, a cloud with  $\sigma$  and  $\Sigma$  offset from  $\sigma^2/R \rightarrow \Sigma$  is in equilibrium with the external pressure  $P_{\text{ext}}$  (and therefore  $V_0^2$  is not constant with  $\Sigma$  but varies depending on  $P_{\text{ext}}$ ; cf. expectation for SVE, where  $\sigma \propto R^{0.5}$ ; see e.g., Heyer et al. 2009; Hughes et al. 2010, 2013; Meidt et al. 2013).

We use the virial parameter, which is defined using Equation 6 and describes the balance between kinetic and gravitational potential energies, to quantify how stable an MC is. An  $\alpha_{\text{vir}} \approx 2$  corresponds to approximately equipartition between the two energy terms and is often used to assess the boundedness of a given structure (see e.g., Kauffmann et al. 2017)<sup>12</sup>.

<sup>12</sup> Note, however, that the true virial state/boundedness of a given structure

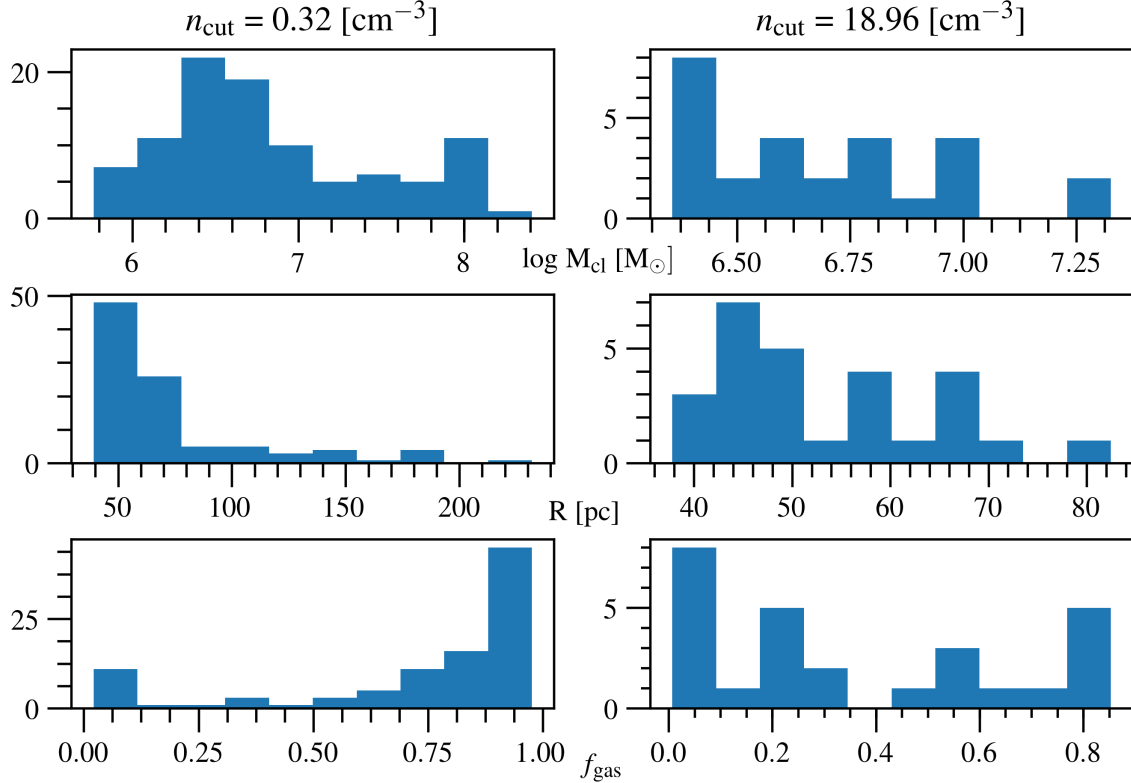


**Figure 4.** Distributions of mass, size, and gas mass fraction of MCs identified using the lowest  $n_{\text{cut}}$  (left panels) and  $n_{\text{cut}} = 18.96 \text{ cm}^{-3}$  (right panels). Note that the scale shown on the y-axes are different between the left and right panels, as less MCs are identified at higher  $n_{\text{cut}}$ .

### 3.2. MC Properties

#### 3.2.1. Single Snapshots

In each snapshot (see Figure 3 for example), we identify a set of MCs with consistently high turbulences and surface densities regardless of the H<sub>2</sub> density cuts adopted. These are the MCs at the center of the main disk of Althæa and occupy the top right corner of the Larson's relation shown in Figure 5. Their velocity dispersions are comparable to those observed in the inner Milky way and nearby gas-rich galaxies (e.g., M64; Oka et al. 2001; Rosolowsky & Blitz 2005; Heyer et al. 2009), along the locus of  $\sigma \propto R^{0.56}$ . Such high velocity dispersions and surface densities are expected since they are located in the nuclear regions of the galaxy, where the potential well is also deeper. The higher velocity dispersions in these MCs can also be understood as they have experienced more recent episodes of star formation as Althæa is assembling its stellar mass (these MCs also have higher stellar-to-gas mass ratios of  $\sim 60$ ). In fact, by  $z \simeq 7.2$  (i.e., the snapshot corresponding to the top panels of Figure 1 and Figure 5), Althæa has assembled a stellar mass of  $M_* = 7.5 \times 10^9 M_{\odot}$ . Thus, the higher velocity dispersion is due in part to the stronger stellar feedback compared to e.g., MCs in its satellite galaxies ( $\sigma \approx 10 \text{ km s}^{-1}$ ).

As we increase the density threshold, some of the MC within the main disk break into multiple sub-MCs. As such,

also depends on the surface terms and the magnetic field (see Equation 5).

we effectively identify a population of denser molecular structures (Figure 3). This population of sub-MCs has dynamics largely similar to those observed in  $z \sim 2$  spatially resolved studies of gas-rich star-forming galaxies, in terms of their velocity dispersions, sizes, and gas surface densities (Figure 5; see e.g., Swinbank et al. 2011), with sizes of the order of  $R \simeq 100 \text{ pc}$  and velocity dispersions of  $\sigma \simeq 20-80 \text{ km s}^{-1}$ . As shown in the top panel of Figure 6, their virial parameter ( $\alpha_{\text{vir}} \gtrsim 10$ ) are lower than their “parent” MCs found in the main disk of Althæa ( $\alpha_{\text{vir}} \gtrsim 100$ ).

We also compare the MCs identified in our simulations to those observed in the Milky Way in the context of the  $\sigma^2/R - \Sigma$  relation (see bottom panel of Figure 6). The V-shaped dashed lines in the figure show the loci along which the given external pressures are needed for MCs to have linewidth for a given set of surface densities (see §3.1).

The lower  $\alpha_{\text{vir}}$  and  $P_{\text{ext}}$  compared to their parent MCs are consistent with the notion that collapsing structures result from local gravitational instability within globally non-collapsing structures (see e.g., Ballesteros-Paredes et al. 2011), which are supported by turbulence and rotation. In fact, based on the virial parameter, velocity dispersion, and pressure of the MC identified in the main disk of Althæa, the MC itself is gravitationally unbound and is supported by turbulence (from the feedback of multiple episodes of star formation) and galactic rotation on large scales (occupying the high pressure region shown in the bottom panel of Figure 6).

The MCs in the satellite galaxies are found to have lower virial parameters compared to the (sub-)MCs in the main disk of Althæa, with  $\alpha_{\text{vir}} \approx 2$ . Differences in their  $\alpha_{\text{vir}}$  most likely result from the weaker stellar feedback in the satellite galaxies as they have experienced less episodes of star formation compared to Althæa (i.e., lower stellar-to-gas mass ratios of  $\sim 0.1$ ). In addition, the MCs in the satellite galaxies follow the locus of  $\log(P/\text{K cm}^{-3}) = 6$  (see bottom panel of Figure 6). Given the low virial parameter and the  $\sigma^2/R - \Sigma$  relation found for these MCs in the satellite galaxies, these structures are likely collapsing structures. This paints a picture, in which star formation continues as gas from the satellite galaxies are being accreted onto the main galaxies during the EoR.

Larson's third relation describes fundamental properties of molecular clouds, relating their structures on small and large scales via two physical properties: mass and size (Larson 1981; McKee & Ostriker 2007). This is also known as the law of constant column density, since cloud mass in observations is sometimes derived by integrating over the mass surface density ( $\Sigma$ ), which is related to the column density ( $N_{\text{H}_2}$ ) obtainable from extinction maps ( $A_V$ ). That is,  $N_{\text{H}_2} \propto A_V$ ,  $\Sigma \propto N_{\text{H}_2}$ , and  $M = \int \Sigma dA$ . Therefore, cloud mass is related to  $N_{\text{H}_2}$  and  $A_V$ .

We show in Figure 12 the size-mass relation of the MCs of Althæa in its accretion phase (see §2.2) compared to observational data of molecular clouds in the Milky Way that are found to be associated with massive star formation (Beuther et al. 2002; Mueller et al. 2002; Hill et al. 2005; Motte et al. 2007) and an empirical relation obtained for massive star formation based on Milky Way clouds ( $< 10 M_\odot$ ; Kauffmann & Pillai 2010; Kauffmann et al. 2010 and references therein):  $M \gtrsim 870 M_\odot \times (r/\text{pc})^{1.33}$ . Kauffmann et al. (2010) interpret this empirical relation as the threshold for massive star formation. The implication of this result is that cluster-forming cloud fragments are found to be more massive than those that are devoid of clusters at a given radius. We also show the loci of constant surface densities in Figure 12, parameterized through the visual extinction  $A_V$ .

As shown in Figure 12, the MCs identified in the accretion phase of Althæa lie above this relation, along the locus with a visual extinction of  $A_V = 4$  mag (Lombardi et al. 2010), which is below the locus of  $A_V = 100$  mag followed by Milky Way clouds. This can be understood by acknowledging the fact that a  $\text{H}_2$  molecular cloud does not necessarily contain CO (e.g., as CO forms deeper in molecular clouds), and that our simulation does not have enough resolution to directly form CO<sup>13</sup>. That is, the MCs of Althæa lying along the locus of  $A_V = 4$  mag likely manifests from the fact that the MCs in our simulation have lower column densities than the star-forming cores observed in the Milky Way, which are observationally well-resolved within an MC, and indeed, have sufficient col-

<sup>13</sup> In fact, to form CO and make predictions for CO line emission in the work presented by Vallini et al. (2018), we model the internal structure of MC within each cell in our simulation.

umn density to form CO.

Similar MC properties in relation to those observed in the nearby Universe are found during the starburst phase of Althæa (see e.g., bottom panel of Figure 5 and Figure 7). On average, we do not find any quantitative differences in the MC properties in the accretion versus starburst phase.

### 3.2.2. Cumulative Mass Distribution

The mass range of the MCs identified in our simulation is  $M_{\text{cl}} \approx 10^{6.5-9} M_\odot$ , which is consistent with those observed in  $z \sim 2$  galaxies in rest-frame UV and optical light (Elmegreen et al. 2007, 2009). Observational studies in the nearby Universe, where spatial resolution are better at revealing molecular (sub-)structures, often report the mass distribution of molecular clouds in the form of a cumulative function (CMF). While the CMF of the MCs for a given snapshot of our simulation is quite noisy, since we have only one (main) galaxy, we can improve the “signal-to-noise ratio” by including MCs identified across all snapshots<sup>14</sup>. We show the resulting CMF in Figure 13.

Motivated by the observational study by Blitz et al. 2007, we fit a power-law to the CMF, which is expressed in the form of:

$$n(M' > M) \propto M_{\text{cl}}^\alpha, \quad (11)$$

where  $n$  is the number of MCs with masses exceeding  $M_{\text{cl}}$  and  $\alpha$  is the power-law index. We find that the slope varies from  $-0.49 \pm 0.01$  to  $-1.17 \pm 0.06$  for the lowest and the highest  $n_{\text{cut}}$  adopted. The uncertainties are the formal fitting uncertainties. Regardless of the density threshold adopted, the slope of the CMF of Althæa (Figure 13) is shallower compared to those observed in nearby galaxies (between  $-1.6$  and  $-2.5$ ; based on a sample of  $\sim 70$  resolved GMCs in M31, M33, IC10 and the Magellanic Clouds; Blitz et al. 2007). This suggests that the MCs of Althæa are more massive compared to those observed in the nearby Universe.

## 4. Discussions and Implications

### 4.1. Variation in MC Properties Depending on the Choice of Density Cuts and Temporal Evolution in Cloud Dynamics

We investigate possible variations in the dynamics of the molecular structures of Althæa and its satellites to test the robustness of our results against the choice of density threshold by adopting different sets of  $n_{\text{cut}}$  in identifying the MCs. That is, how sensitive are the structure properties, and thus, the results presented in §3.2.1 dependent on the choice of density thresholds. We vary the choice of  $\text{H}_2$  density for each of the snapshots and find no obvious differences in our results (i.e., inferences on the dynamics of  $z \sim 6$  MCs in relation to those observed in nearby and  $z \sim 2$  galaxies in the context of cloud scaling relations). In addition, for the densest MC in the main

<sup>14</sup> This approach is valid unless in some snapshots, the galaxy experience a violent event, which is relatively rare across the 700 Myr studied here.

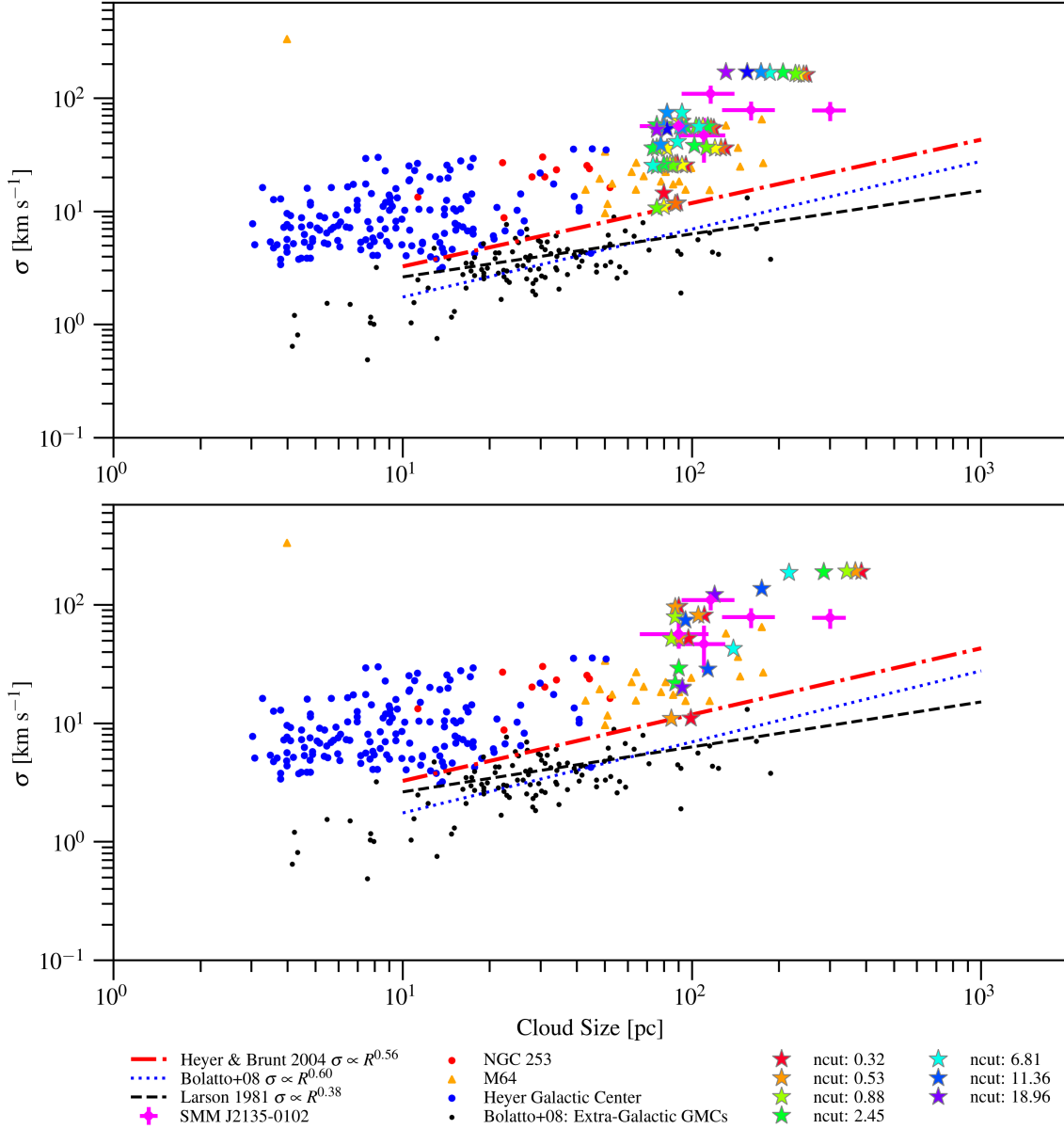


**Figure 5.** Larson’s (linewidth-size) relation of Althaea in accretion phase (top) and starburst phase (bottom) compared to those observed in nearby and the  $z \sim 2$  star-forming galaxy. Literature data and empirical relations are compiled from Larson (1981); Heyer & Brunt (2004); Rosolowsky & Blitz (2005); Bolatto et al. (2008); Swinbank et al. (2011); Leroy et al. (2015).

disk of Althaea, we find that while its size decreases as we increase  $n_{\text{cut}}$  — as one would intuitively expect, its velocity dispersion remain approximately  $\sigma \simeq 200 \text{ km s}^{-1}$  (see Figure 5). This lack of variation is reassuring, in the sense that at least on the scales studied here, the dynamics of the MCs are not artifacts or biased by our choice of  $n_{\text{cut}}$ . Our results are therefore robust to the various density cuts of choice.

We show the properties of all MCs identified across all snapshots in Figure 8, Figure 9, Figure 10, and Figure 11. We find no quantitative differences in the cloud properties over the 700 Myr traced in our simulation.

#### 4.2. Origin of the MCs

The largest molecular structure identified is essentially the main disk of Althaea which breaks down into smaller substructures that are denser as we increase  $n_{\text{cut}}$  (see e.g., Figure 9 and Figure 11). In any case, the MCs we identified are much bigger in size and mass than nearby GMCs, which is consistent with those observed in  $z \sim 2-4$  galaxies based on spatially resolved imaging (Swinbank et al. 2011).

The high pressure observed in Althaea is also comparable to what has been observed in local ULIRGs; however, the molecular clouds in the latter are concentrated within their central regions and have typical sizes of  $\sim 70-100 \text{ pc}$  and masses on the order of  $\sim 10^9 M_{\odot}$  (Downes & Solomon 1998; Sakamoto et al. 2008). In our simulation, the high pressure MCs of Althaea are found throughout the disk. This difference

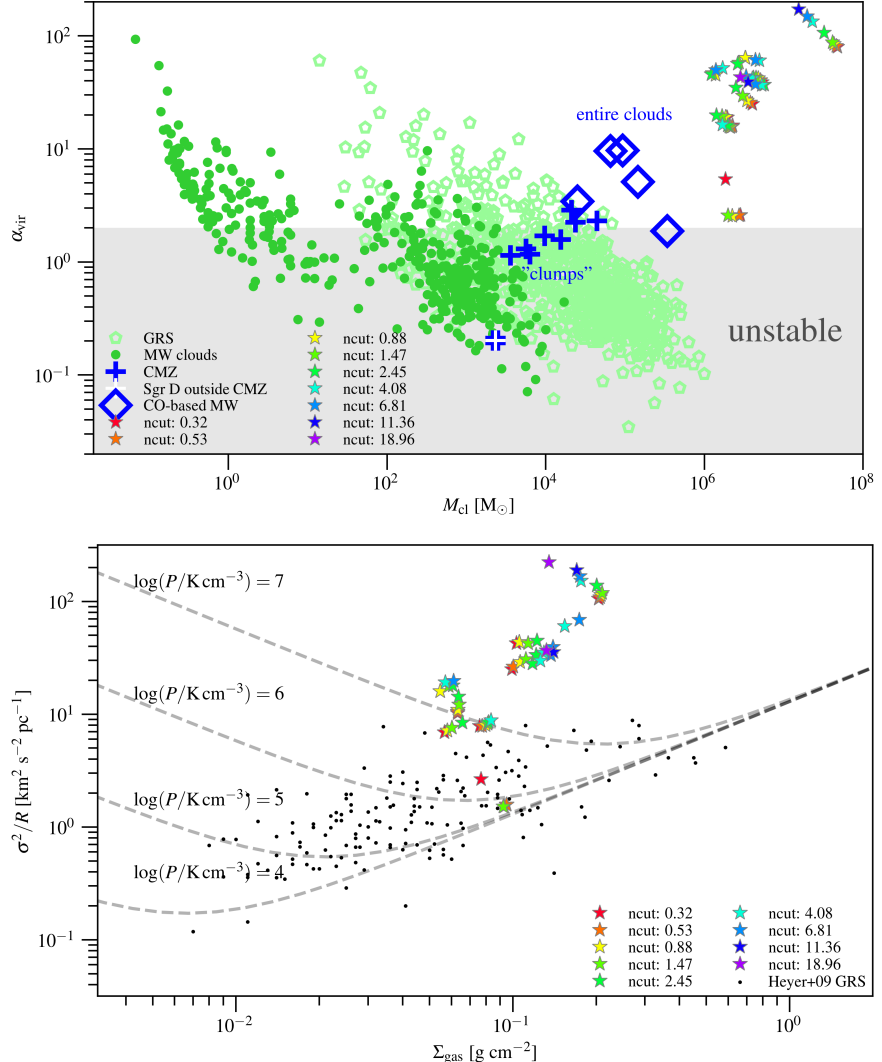


**Figure 6.** Top: Virial parameter and cloud mass of Althaea in the accretion phase (star symbols) compared to those observed in the Milky Way (other symbols). Literature data are compiled from Kauffmann et al. 2017 and references therein. Bottom:  $\sigma^2/R - \Sigma_{\text{gas}}$  relation of the MCs identified in our simulation (star symbols) compared to those observed in the Milky Way (black dot markers; Heyer et al. 2009). The V-shaped dashed lines show the loci along which the given external pressures are needed for MCs to have linewidth  $\sigma$  for a given set of surface densities (see §3.1). In both panels, the star symbols are color-coded by  $n_{\text{cut}}$ . Star symbols lying close to  $\alpha_{\text{vir}} \approx 2$  in the top panel and the locus of  $\log(P/\text{K cm}^{-3}) = 6$  in the bottom panel correspond to MCs identified in the satellite galaxies.

likely stems from the different physical mechanisms giving rise to the formation (and thus the nature) of these molecular structures. For instance, in local ULIRGs, they are probably form by shock compression or cloud-cloud collision after the large amount of gas from the progenitor galaxy merger is being funneled toward the central region (Tan 2000; Wu et al. 2018), whereas in Althaea, which is actively accreting gaseous materials from the surrounding, they are probably form from constant cold gas accretion onto the entire galaxy (without requiring gas to be funneled into the central region). This latter mechanism may also be the dominant mode for forming the highly supersonic massive MCs observed in gas-rich star-forming galaxies at  $z \sim 2$  (see also e.g., Swinbank et al. 2011). The constant inter-cloud collision as gas is being accreted onto the main galaxy would also render the MCs to be gravitationally unbound (see e.g., Dobbs et al. 2011), which

would be consistent with/explain the high  $\alpha_{\text{vir}}$  found for the MCs in the main disk of Althaea.

#### 4.3. Virial Parameter, Collapse, and high SFR at high- $z$

While it may appear that there is an inconsistency between the high  $\alpha_{\text{vir}}$  nature of the majority of the molecular gas in Althaea and its SFR. That is, if most of the molecular gas in Althaea has high  $\alpha_{\text{vir}}$ , why does it sustain its high SFR of  $\sim 100 M_{\odot} \text{ yr}^{-1}$ ? This discrepancy can be explained in two ways. First, our results are limited by the resolution of the simulation, such that, in each MC, there likely exist multiple smaller-scales molecular structures (e.g., clumps and cores), as in the classical MC hierarchy. Second, due to turbulence dissipation on small-scales, such (sub-)structures are no longer supported by large-scale gravitational potential and differential rotation. This in turn enables subregions of the

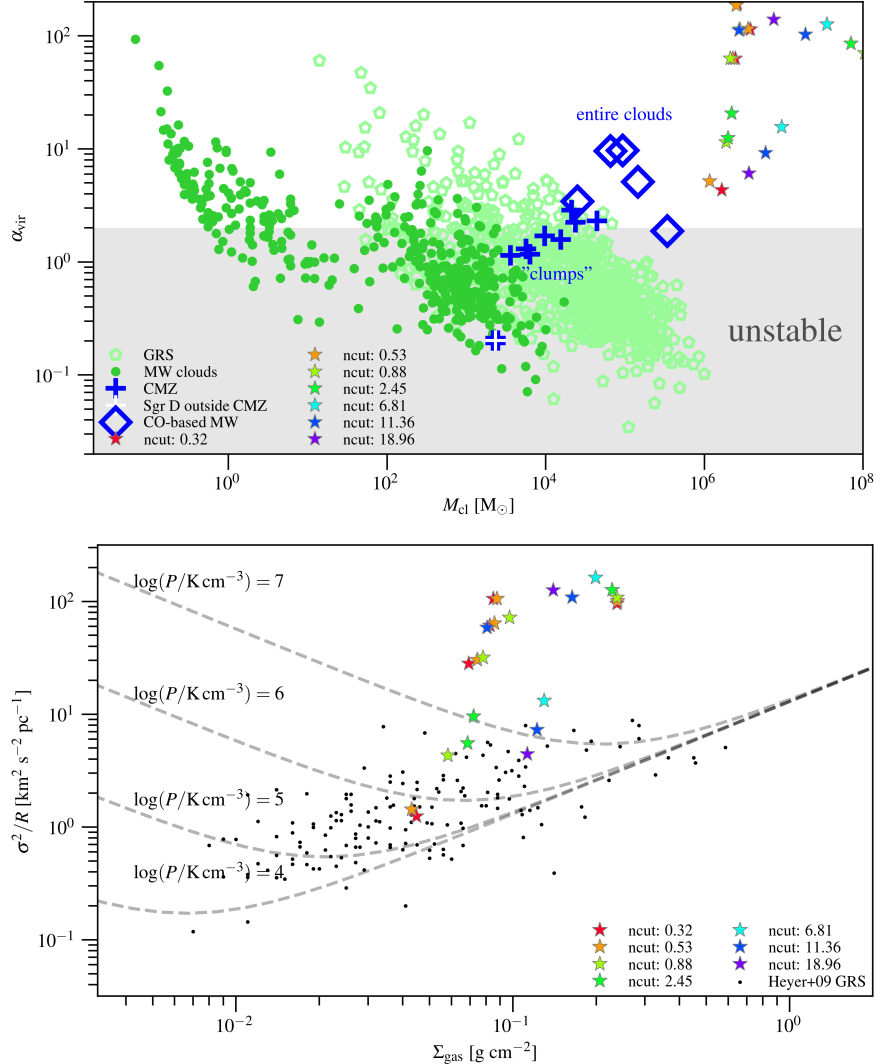


**Figure 7.** Same as Figure 6, but for MCs identified in the starburst phase of Althæa.

MCs to collapse and potentially form OB associations out of these unbound MCs (Clark & Bonnell 2004; Clark et al. 2005). Additional mechanisms causing non-axisymmetric perturbations (e.g., arms) to the gravitational potential can also induce orbit crossing, shocks and dissipation in gas, further promoting turbulence dissipation.

We note that in a recent study by Pettitt et al. (2018), the authors report that the virial parameter could be a poor indicator for the star-forming capacity of the massive ( $10^5\text{--}6 M_\odot$ ) “clouds” in their simulation. In particular, these authors do not find any significant correlations between the virial parameter, cloud mass, and star formation efficiency ( $M_*/M_{\text{cl}}$ ). Identifying a new diagnostic tool is beyond the scope of this paper. Here, we are more interested in comparing the clouds dynamics with observational studies, and thus, part of the discussion of this paper is based on virial analysis.

#### 4.4. MC Dynamics and CMF and IMF at EoR

Velocity dispersion and surface density are tightly connected to pressure. That is, the pressure of an MC is expected

to increase with its velocity dispersion and surface density (see e.g., Equation 9 and since  $P \propto \Sigma^2$ ). In the central molecular zone of the Milky Way (CMZ), we have seen molecular clouds with high pressures of  $P/k_B > 10^7 \text{ K cm}^{-3}$ . Such high pressures are also seen in massive star-forming regions such as 30 Doradus. The higher  $\Sigma_{\text{gas}}$  in turn is related to more massive clouds being formed. In M64 and M51, there are a few clouds with masses  $M_{\text{cl}} > 10^7 M_\odot$  (Rosolowsky & Blitz 2005; Koda et al. 2009; Colombo et al. 2014). On the other hand, such massive molecular structures are unknown to Local Group galaxies (e.g., Rice et al. 2016), and are likely the sites from which massive star clusters or OB associations are to be formed. The shallower slope found in the CMF for Althæa compared to those observed in the nearby Universe (see §3.2.2) may suggest that the MCs of Althæa are more massive compared to those observed in the nearby Universe, notwithstanding the limited numerical resolution of our simulation. That said, the Jeans mass  $M_J = \sigma^4/(G^2\Sigma)$  yields  $\sim 8 \times 10^8 M_\odot$  for a velocity dispersion of  $\sigma \approx 50 \text{ km s}^{-1}$  and a gas mass sur-

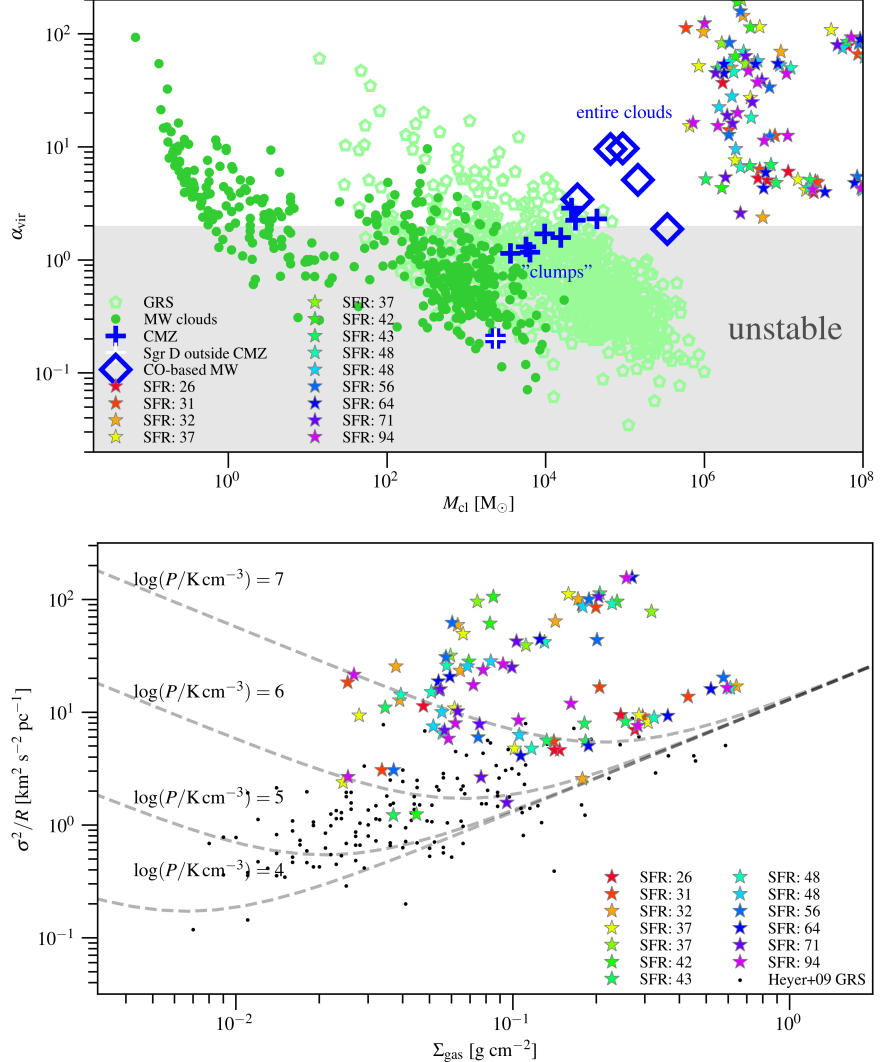


**Figure 8.** Same as Figure 6, but for MCs identified across all snapshots. Star symbols are color-coded by increasing SFR.

face density of  $\Sigma_{\text{gas}} \approx 450 M_{\odot} \text{ pc}^{-2}$ , which are typical of the MCs of Althæa. This Jeans mass is in agreement with the mass range found (see Figure 4).

The CMF is related to the mass function of stars (IMF), since the former describes the mass distribution of the materials for star formation (see e.g., McKee & Ostriker (2007) for a review). Observational studies of a diverse range of environments suggest that the IMF is invariant between star-forming regions, star clusters, and spiral galaxies (see a review by Bastian et al. 2010; see also Bochanski et al. 2010; Alves de Oliveira 2013; Calamida et al. 2015), but is subject to variation under extreme conditions (e.g., temperatures, densities, and radiation field intensities), such as in the Galactic center (e.g., Lu et al. 2013; Conroy et al. 2013). Speculatively, the different CMF slope found in Althæa may suggest a different IMF compared to those observed in nearby galaxies. In particular, the steeper slope may indirectly translate into a top-heavy IMF (see Alves et al. 2007; Anathpindika 2011),

which is commonly assumed in most high- $z$  studies to date<sup>15</sup>.

One should, however, keep in mind that the slope of the CMF reported here is subject to the uncertainties in the analysis method and limitations in the numerical resolution of our simulation. That is, we are likely biased to finding more massive clouds due to resolution effects; it is possible that we may identify more less massive MCs if our simulation was done at a higher resolution. That said, one must acknowledge that such a zoom-in simulation is currently quite expensive to perform with existing computational power. In any case, similarly massive molecular clouds have been reported in idealized closed-box isolated galaxy simulations done at higher resolution (e.g., Behrendt et al. 2016). Note, however, that the IGM and merger and accretion histories are not properly modeled in such simulations since they adopt non-cosmological initial conditions. It is therefore conceivable that our results are not that far off in spite of the limited resolution ( $l \approx 30 \text{ pc}$ ).

<sup>15</sup> Since intuitively, we expect a higher Jeans mass at higher redshift, due to the lower metallicities and higher temperature expected in these first galaxies.

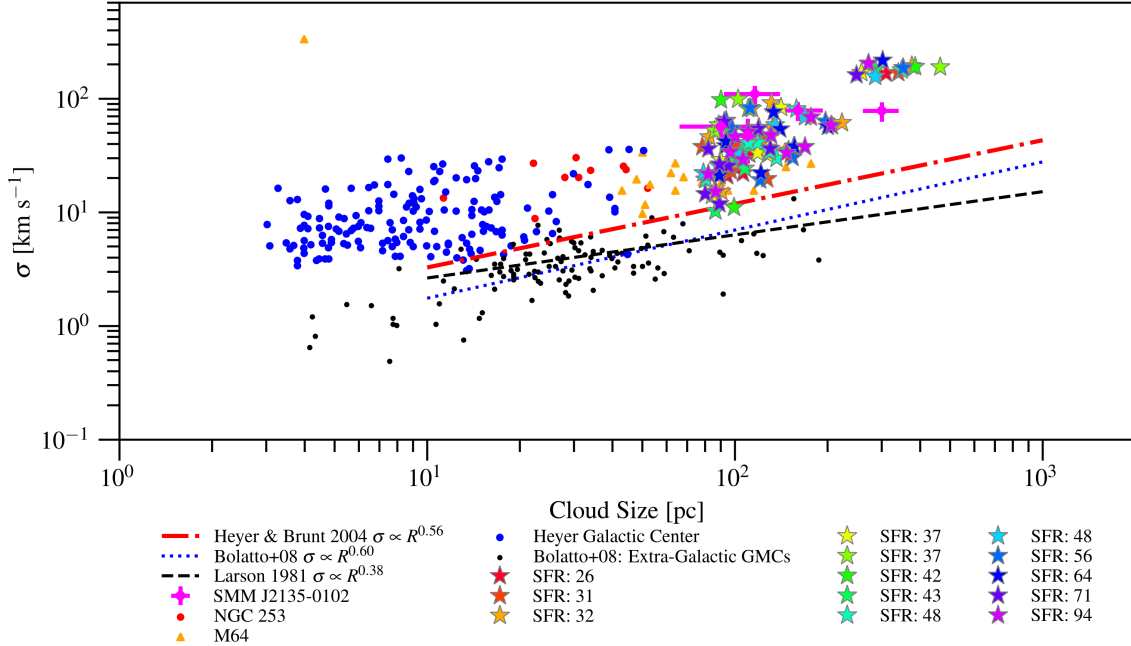


**Figure 9.** Comparison of the MCs of Althaea identified across all snapshots over the course of 700 Myr (star symbols) to those observed in nearby and the  $z \sim 2$  star-forming galaxy in the context of the linewidth-size relation — showing variations in their properties at the different evolutionary phases of Althaea and with varying SFRs.

Future higher resolution zoom-in simulations would certainly be useful to understand the evolving dynamical properties of the lower-mass molecular structures in galaxies at EoR under the influence of gas inflow/outflow (i.e., accounting for energy injection at large scale due to infall/outflow).

## 5. Summary and Conclusions

We study the dynamical properties of molecular clouds complexes and their temporal evolution in a  $z \sim 6$  prototypical galaxy at the EoR using state-of-the-art cosmological zoom-in simulation (SERRA), which includes a chemical network to determine the formation of molecular hydrogen, heating and cooling of the ISM by metals, and stellar feedback. We use a clump-finding algorithm and a set of H<sub>2</sub> volumetric densities to identify MCs and their sub-structures in the main galaxy of the simulated 20 Mpc  $h^{-1}$  box — Althaea — and in its satellites. We decompose the molecular structures into non-overlapping tiles by identifying a set of different density contours at different snapshots. Using volumetric H<sub>2</sub> is essentially similar to identifying molecular structures using different contour levels/surfaces on surface brightness maps/cubes of molecular line tracers (e.g., CO, CS, NH<sub>3</sub>), since the line luminosity scales with the molecular gas density (modulo optical depth effects). We extract properties such as mass, size, Mach number, velocity dispersion, gas surface density, and virial parameter for each MC and compare them with those observed in the Milky Way disk, the Galactic center, and gas-rich starburst galaxies in the local Universe and at the peak epoch of cosmic star formation. We also examine their properties at the different evolutionary stages of Althaea and compare them with observations.

We find that the MC of Althaea are highly supersonic, with high velocity dispersions ( $\sigma \approx 200 \text{ km s}^{-1}$ ) comparable to those observed in  $z \sim 2$  starburst galaxies. The mass scale of the MCs is of the order of  $10^{6.5-9} M_{\odot}$ . The  $\sim 200 \text{ pc}$ -scale MCs found with a low density threshold correspond to the arms of the disk of Althaea which break down into smaller  $\lesssim 100 \text{ pc}$ -scale MCs at higher density thresholds. The more massive and bigger MCs in Althaea compared to the Milky Way likely result from the higher gas mass fraction, surface density, and velocity dispersion, which set the scale for fragmentation. This is consistent with what has been found previously in higher resolution idealized simulation of isolated galaxies. That said, our cosmological zoom-in simulation here allows us to examine the influence on the dynamics of MCs due to continuous gas accretion from the surrounding IGM (see e.g., Klessen & Hennebelle 2010; Goldbaum et al. 2011).

We compare the dynamics of MCs in Althaea to observations in the context of the Larson's relation. The MCs of Althaea are found to have higher  $\sigma$  and  $\Sigma$  systematically regardless of the  $n_{\text{cut}}$  adopted. Our results are thus insensitive to the various density cuts of choice. The velocity dispersion remains  $\gtrsim 100 \text{ km s}^{-1}$  even when we increase the  $n_{\text{cut}}$  and even for the molecular substructures. Such a high velocity dispersion likely results from the strong supernova and stellar feedback Althaea experienced over the multiple episodes of bursty star formation. Virial analysis indicates that the MC/arms of the main disk of Althaea are unbound, but the substructures have lower virial parameter. This is consistent with the notion that collapsing structures result from gravitational instability within globally stable structures, which are supported by tur-

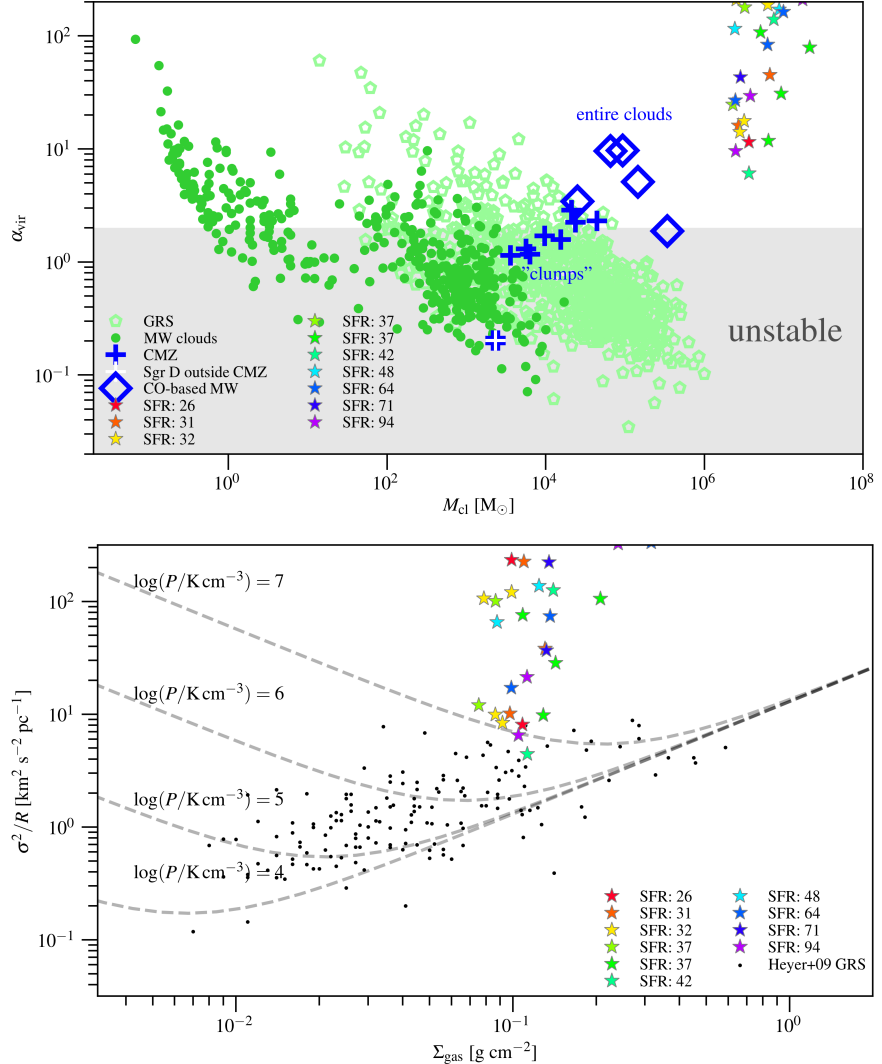


**Figure 10.** Same as Figure 8, but only the denser substructures of the main disk of Althaea are included (i.e., MCs here are identified with the highest  $n_{\text{cut}}$ ).

bulence and rotation on large scale. We also find  $\alpha_{\text{vir}} \approx 2$  for the MCs in the satellite galaxies, which we interpret as result of the weaker stellar feedback as they have experienced less episodes of star formation compared to Althaea (also supported by the lower stellar-to-gas mass ratio of the latter). MCs in the satellites are therefore likely collapsing structures. This paints a picture, in which at the EoR, star formation continues as gas is being accreted from the IGM.

We find no temporal variations in the MC dynamics over the course of 700 Myr traced in our simulation, at least in terms of the scaling relations examined. Our results are independent of the volume density threshold adopted, except for the slope of the cumulative mass distribution, which steepens as we increase  $n_{\text{cut}}$ .

Determining the multi-phase ISM properties of early galaxies is a critical piece to understanding the evolution and assembly history of galaxies, since they set the pace for chemical reactions and excitation rates for the coolants in the ISM (and subsequent star formation). Observations leveraging the

combination of spatial-spectral imaging of multi-band continuum and spectral line emission are crucial for better understanding the role of high- $z$  galaxy populations in the context of galaxy evolution and the ISM physics behind their intense star formation in the early Universe. High resolution zoom-in simulations, such as SERRA, while inherently limited in galaxy statistics and is subject to the input model/sub-grid models adopted, provide an avenue to examine and postulate/make testable predictions on the morphology and dynamics of the multi-phase ISM structures of the first galaxies and their satellite galaxies. High resolution imaging of the molecular gas content in the first galaxies with ALMA and the ngVLA, on the other hand, have the potential to provide useful observational data to test our findings and the validity of our simulation to shed light on star formation since the cosmic dark ages.

We thank Jens Kauffmann, Thushara Pillai, and Mark Swinbank for sharing their data. T.K.D.L. acknowledges sup-

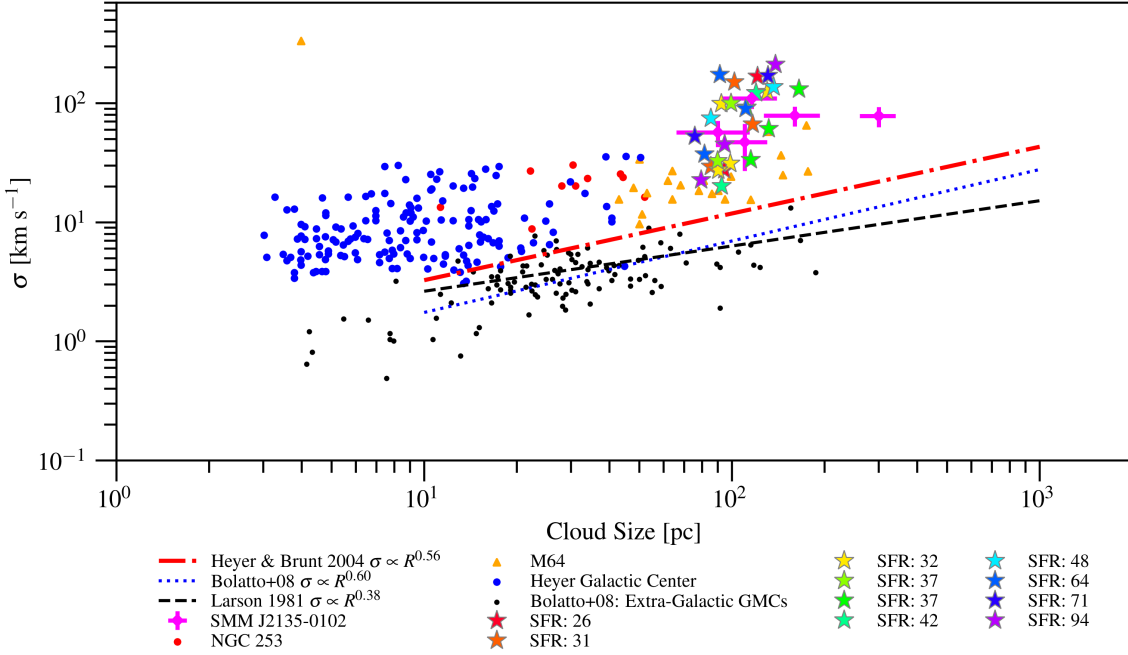


**Figure 11.** Same as Figure 9, but only the denser substructures of the main disk of Althaea are included (i.e., MCs here are identified with the highest  $n_{\text{cut}}$ ).

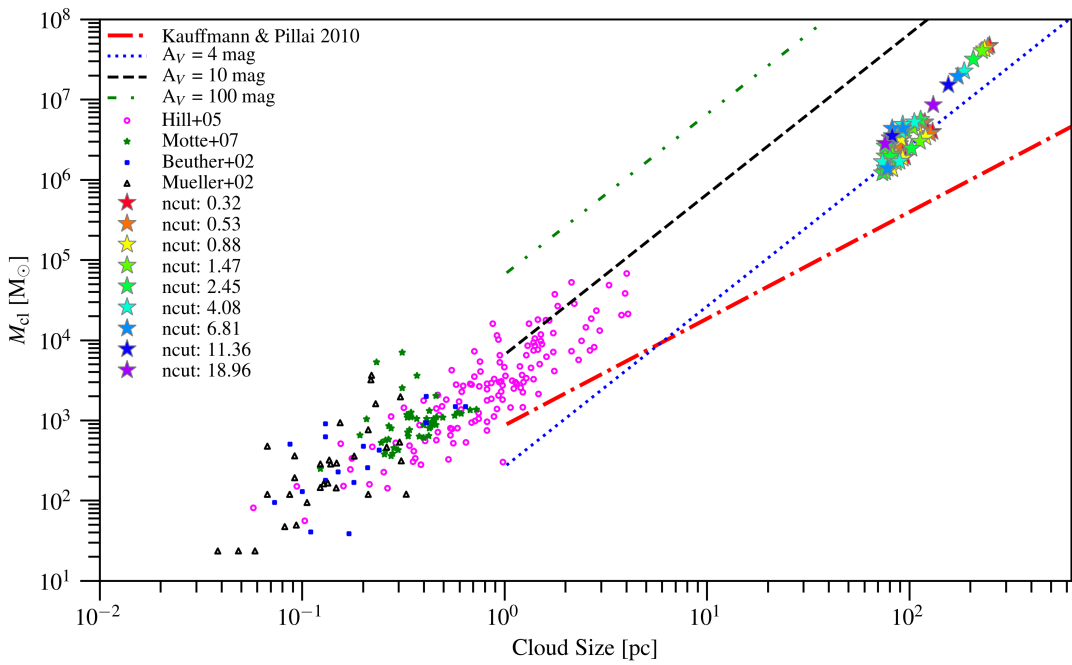


**Figure 12.** Size-mass relation of MCs identified in the accretion phase of Althaea in our simulation (star symbols) compared to observational data of molecular clouds in the Milky Way associated with massive star formation (magenta circles, green stars, blue dots, and black triangles) and empirical relations established based on observations of the Milky Way. Red line shows the threshold for massive star formation reported by Kauffmann & Pillai (2010). Star symbols are color-coded by increasing  $n_{\text{cut}}$ . Literature data are compiled from Beuther et al. (2002); Mueller et al. (2002); Hill et al. (2005); Motte et al. (2007). The colored lines show the loci expected for various visual extinctions ( $A_V$ ), which corresponds to lines of constant surface density (i.e., Larson's third relation). This representation is motivated by observational studies (see text and e.g., Lombardi et al. 2010).

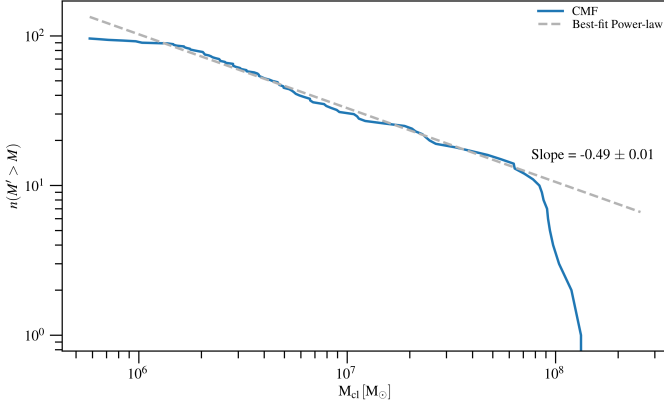


**Figure 13.** CMF of MCs in Althaea and best-fit power law.

port by the NSF through award SOSP4-009 from the NRAO

and support from the Simons Foundation. A.F. acknowledges support from the ERC Advanced Grant INTERSTELLAR H2020/740120. This work is based on a project developed at the Kavli Summer Program in Astrophysics (KSPA) held at the Center for Computational Astrophysics of the Flatiron Institute in 2018. The program was co-funded by the Kavli Foundation and the Simons Foundation. We thank the KSPA Scientific and Local Organizing Committees, and the program founder, Pascale Garaud, for supporting the genesis of this work. We also thank the Center for Cosmology and Particle Physics at the New York University for their hospitality in hosting us after the steam pipe explosion in NYC during the KSPA. This research has made use of NASA's Astrophysics Data System Bibliographic Services and YT, a community-developed Python package for analyzing simulation data in Astronomy.

- Alves, J., Lombardi, M., & Lada, C. J. 2007, *A&A*, **462**, L17  
 Alves de Oliveira, C. 2013, *Mem. Soc. Astron. Italiana*, **84**, 905  
 Anathpindika, S. 2011, *New A*, **16**, 477  
 Ballesteros-Paredes, J., Hartmann, L. W., Vázquez-Semadeni, E., Heitsch, F., & Zamora-Avilés, M. A. 2011, *MNRAS*, **411**, 65  
 Ballesteros-Paredes, J., & Mac Low, M.-M. 2002, *ApJ*, **570**, 734  
 Bastian, N., Covey, K. R., & Meyer, M. R. 2010, *ARA&A*, **48**, 339  
 Beaumont, C. N., Offner, S. S. R., Shetty, R., Glover, S. C. O., & Goodman, A. A. 2013, *ApJ*, **777**, 173  
 Behrendt, M., Burkert, A., & Schartmann, M. 2016, *ApJ*, **819**, L2  
 Behroozi, P. S., Wechsler, R. H., & Conroy, C. 2013, *ApJ*, **770**, 57  
 Beuther, H., Schilke, P., Menten, K. M., et al. 2002, *ApJ*, **566**, 945  
 Blitz, L., Fukui, Y., Kawamura, A., et al. 2007, *Protostars and Planets V*, 81  
 Bochanski, J. J., Hawley, S. L., Covey, K. R., et al. 2010, *AJ*, **139**, 2679  
 Bolatto, A. D., Leroy, A. K., Rosolowsky, E., Walter, F., & Blitz, L. 2008, *ApJ*, **686**, 948  
 Bouwens, R. J., Illingworth, G. D., Labbe, I., et al. 2011, *Nature*, **469**, 504  
 Bovino, S., Grassi, T., Capelo, P. R., Schleicher, D. R. G., & Banerjee, R. 2016, *A&A*, **590**, A15  
 Calamida, A., Sahu, K. C., Casertano, S., et al. 2015, *ApJ*, **810**, 8  
 Carniani, S., Maiolino, R., Amorin, R., et al. 2018, *MNRAS*, **478**, 1170  
 Ceverino, D., Dekel, A., & Bournaud, F. 2010, *MNRAS*, **404**, 2151  
 Clark, P. C., & Bonnell, I. A. 2004, *MNRAS*, **347**, L36  
 Clark, P. C., Bonnell, I. A., Zinnecker, H., & Bate, M. R. 2005, *MNRAS*, **359**, 809  
 Colombo, D., Hughes, A., Schinnerer, E., et al. 2014, *ApJ*, **784**, 3  
 Conroy, C., Dutton, A. A., Graves, G. J., Mendel, J. T., & van Dokkum, P. G. 2013, *ApJ*, **776**, L26  
 Dobbs, C. L., Burkert, A., & Pringle, J. E. 2011, *MNRAS*, **413**, 2935  
 D'Odorico, V., Feruglio, C., Ferrara, A., et al. 2018, *ApJ*, **863**, L29  
 Downes, D., & Solomon, P. M. 1998, *ApJ*, **507**, 615  
 Dunlop, J. S., McLure, R. J., Biggs, A. D., et al. 2017, *MNRAS*, **466**, 861  
 Elmegreen, B. G., Elmegreen, D. M., Fernandez, M. X., & Lemoine, J. J. 2009, *ApJ*, **692**, 12  
 Elmegreen, D. M., Elmegreen, B. G., Ravindranath, S., & Coe, D. A. 2007, *ApJ*, **658**, 763  
 Federrath, C., & Klessen, R. S. 2013, *ApJ*, **763**, 51  
 Ferkhoff, C., Brisbin, D., Nikola, T., et al. 2015, *ApJ*, **806**, 260  
 Gabor, J. M., & Bournaud, F. 2013, *MNRAS*, **434**, 606  
 Goldbaum, N. J., Krumholz, M. R., Matzner, C. D., & McKee, C. F. 2011, *ApJ*, **738**, 101  
 Goldreich, P., & Lynden-Bell, D. 1965, *MNRAS*, **130**, 125  
 Goodman, A. A., Alves, J., Beaumont, C. N., et al. 2014, *ApJ*, **797**, 53  
 Grassi, T., Bovino, S., Schleicher, D. R. G., et al. 2014, *MNRAS*, **439**, 2386  
 Heitsch, F., Ballesteros-Paredes, J., & Hartmann, L. 2009, *ApJ*, **704**, 1735  
 Heyer, M., Krawczyk, C., Duval, J., & Jackson, J. M. 2009, *ApJ*, **699**, 1092  
 Heyer, M. H., & Brunt, C. M. 2004, *ApJ*, **615**, L45  
 Hill, T., Burton, M. G., Minier, V., et al. 2005, *MNRAS*, **363**, 405  
 Hodge, J. A., Riechers, D., Decarli, R., et al. 2015, *ApJ*, **798**, L18  
 Hodge, J. A., Swinbank, A. M., Simpson, J. M., et al. 2016, *ApJ*, **833**, 103  
 Hopkins, P. F., Kocevski, D. D., & Bundy, K. 2014, *MNRAS*, **445**, 823  
 Hughes, A., Wong, T., Ott, J., et al. 2010, *MNRAS*, **406**, 2065  
 Hughes, A., Meidt, S. E., Colombo, D., et al. 2013, *ApJ*, **779**, 46  
 Inoue, S., Dekel, A., Mandelker, N., et al. 2016, *MNRAS*, **456**, 2052  
 Kauffmann, J., & Pillai, T. 2010, *ApJ*, **723**, L7  
 Kauffmann, J., Pillai, T., Shetty, R., Myers, P. C., & Goodman, A. A. 2010, *ApJ*, **716**, 433  
 Kauffmann, J., Pillai, T., Zhang, Q., et al. 2017, *A&A*, **603**, A90  
 Kennicutt, Jr., R. C. 1989, *ApJ*, **344**, 685  
 Klessen, R. S., & Hennebelle, P. 2010, *A&A*, **520**, A17  
 Koda, J., Scoville, N., Sawada, T., et al. 2009, *ApJ*, **700**, L132  
 Krumholz, M. R., McKee, C. F., & Tumlinson, J. 2009, *ApJ*, **693**, 216  
 Larson, R. B. 1981, *MNRAS*, **194**, 809  
 Leroy, A. K., Bolatto, A. D., Ostriker, E. C., et al. 2015, *ApJ*, **801**, 25  
 Li, Y., Mac Low, M.-M., & Klessen, R. S. 2005, *ApJ*, **626**, 823  
 —, 2006, *ApJ*, **639**, 879  
 Lombardi, M., Alves, J., & Lada, C. J. 2010, *A&A*, **519**, L7  
 Lu, J. R., Do, T., Ghez, A. M., et al. 2013, *ApJ*, **764**, 155  
 Maiolino, R., Carniani, S., Fontana, A., et al. 2015, *MNRAS*, **452**, 54  
 Malhotra, S., Kaufman, M. J., Hollenbach, D., et al. 2001, *ApJ*, **561**, 766  
 McKee, C. F., & Ostriker, E. C. 2007, *ARA&A*, **45**, 565  
 Meidt, S. E., Schinnerer, E., García-Burillo, S., et al. 2013, *ApJ*, **779**, 45

- Motte, F., Bontemps, S., Schilke, P., et al. 2007, *A&A*, **476**, 1243
- Mueller, K. E., Shirley, Y. L., Evans, II, N. J., & Jacobson, H. R. 2002, *ApJS*, **143**, 469
- Oka, T., Hasegawa, T., Sato, F., et al. 2001, *ApJ*, **562**, 348
- Ono, Y., Ouchi, M., Curtis-Lake, E., et al. 2013, *ApJ*, **777**, 155
- Pallottini, A., Ferrara, A., Bovino, S., et al. 2017a, *MNRAS*, **471**, 4128
- Pallottini, A., Ferrara, A., Gallerani, S., et al. 2017b, *MNRAS*, **465**, 2540
- Pan, H.-A., Fujimoto, Y., Tasker, E. J., et al. 2015, *MNRAS*, **453**, 3082
- Pettitt, A. R., Egusa, F., Dobbs, C. L., et al. 2018, *MNRAS*, **480**, 3356
- Planck Collaboration, Ade, P. A. R., Aghanim, N., et al. 2014, *A&A*, **571**, A16
- Rice, T. S., Goodman, A. A., Bergin, E. A., Beaumont, C., & Dame, T. M. 2016, *ApJ*, **822**, 52
- Rosolowsky, E., & Blitz, L. 2005, *ApJ*, **623**, 826
- Rosolowsky, E., & Leroy, A. 2006, *PASP*, **118**, 590
- Rosolowsky, E. W., Pineda, J. E., Kauffmann, J., & Goodman, A. A. 2008, *ApJ*, **679**, 1338
- Rubin, R. H. 1985, *ApJS*, **57**, 349
- Sakamoto, K., Wang, J., Wiedner, M. C., et al. 2008, *ApJ*, **684**, 957
- Sanders, D. B., Scoville, N. Z., & Solomon, P. M. 1985, *ApJ*, **289**, 373
- Scoville, N. Z., & Solomon, P. M. 1974, *ApJ*, **187**, L67
- Shetty, R., Collins, D. C., Kauffmann, J., et al. 2010, *ApJ*, **712**, 1049
- Smith, B. D., Turk, M. J., Sigurdsson, S., O'Shea, B. W., & Norman, M. L. 2009, *ApJ*, **691**, 441
- Sparre, M., Hayward, C. C., Springel, V., et al. 2015, *MNRAS*, **447**, 3548
- Swinbank, A. M., Papadopoulos, P. P., Cox, P., et al. 2011, *ApJ*, **742**, 11
- Tan, J. C. 2000, *ApJ*, **536**, 173
- Teyssier, R. 2002, *A&A*, **385**, 337
- Toomre, A. 1964, *ApJ*, **139**, 1217
- Turk, M. J., Smith, B. D., Oishi, J. S., et al. 2011, *ApJS*, **192**, 9
- Vallini, L., Pallottini, A., Ferrara, A., et al. 2018, *MNRAS*, **473**, 271
- Williams, J. P., de Geus, E. J., & Blitz, L. 1994, *ApJ*, **428**, 693
- Wu, B., Tan, J. C., Nakamura, F., Christie, D., & Li, Q. 2018, *PASJ*, **70**, S57